


RESEARCH ARTICLE

# A novel morphing soft robot design to minimize deviations

Varell Ferrandy<sup>1</sup>, Arnau Garriga-Casanovas<sup>1</sup>, Enrico Franco<sup>1</sup>, Indrawanto<sup>2</sup>,  
Ferdinando Rodriguez y Baena<sup>1</sup>, Andi Isra Mahyuddin<sup>3</sup> and Vani Viridyawan<sup>2</sup> 

<sup>1</sup>The Hamlyn Centre, Mechanical Engineering, Imperial College London, London SW7 2AZ, UK

<sup>2</sup>Engineering Design and Production Research Group, Faculty of Mechanical and Aerospace Engineering - Institut Teknologi Bandung, Bandung, Indonesia

<sup>3</sup>Dynamics and Control Research Group, Faculty of Mechanical and Aerospace Engineering - Institut Teknologi Bandung, Bandung, Indonesia

**Corresponding author:** Vani Viridyawan; Email: [vani.viridyawan@itb.ac.id](mailto:vani.viridyawan@itb.ac.id)

**Received:** 7 February 2024; **Revised:** 5 July 2024; **Accepted:** 21 August 2024

**Keywords:** soft pneumatic actuator; design optimization; finite element analysis; manufacturing; artificial neural network

## Abstract

Soft robotics is rapidly advancing, particularly in medical device applications. A particular miniaturized manipulator design that offers high dexterity, multiple degrees-of-freedom, and better lateral force rendering than competing designs, has great potential for minimally invasive surgery. However, it faces challenges such as the tendency to suddenly and unpredictably deviate in bending plane orientation at higher pressures. In this work, we identified the cause of this deviation as the buckling of the partition wall and proposed design alternatives along with their manufacturing process to address the problem without compromising the original design features. In both simulation and experiment, the novel design managed to achieve a better bending performance in terms of stiffness and reduced deviation of the bending plane. We also developed an artificial neural network-based inverse kinematics model to further improve the performance of the prototype during vectorization. This approach yielded mean absolute errors in orientation of the bending plane below 5°.

## 1. Introduction

Soft robotics is a rapidly advancing field of research with immense potential to revolutionize various applications, namely search and rescue operations [1, 2], field and inspection tasks [3–5], and most notably, medical devices [6–9]. Over the past two decades, various designs of fluid-actuated soft robotic manipulators have been leading to significant advancements and improved performance, such as a higher number of degrees-of-freedom (DOFs) [10, 11], better bending versus pressure performance, and more recently higher lateral forces [12–14]. Model-based control for these robots has also been proposed [15, 16], with formulations accounting for time-varying disturbances [17], and including pressure dynamics [18]. Control of a 2-segment robot is proposed in [19]. Reinforcement learning approaches to control have also been developed [20, 21]. These developments have propelled the field of fluid-actuated soft robotics toward creating safer and more affordable medical tools for various medical interventions and diagnoses, including minimally invasive surgery (MIS).

A particular miniaturized manipulator design [11, 13, 14] is well-suited for MIS procedures since it offers high dexterity, multiple DOFs, and significant lateral forces that reach approximately 3N per segment with a 12 mm outer diameter, and thus approximately 1N for a three segment robotic manipulator. This is crucial in MIS, which demands substantial forces within a limited, dynamically changing, and unstructured workspace [22]. The performance of this design in terms of force and dexterity is the highest among serial soft robotic manipulators [13], and it is attributed in part to its utilization of a morphing inner structure that changes during pressurization. While offering the above advantages,

this design has been observed to encounter certain challenges, including variations in bending stiffness when pressurized in different chambers, as well as a noticeable deviation in the bending plane at higher pressures. These challenges have been associated with a less predictable movement of the manipulator, as reported in [14]. Addressing these challenges would lead to a manipulator design that not only has the aforementioned advantages for MIS but also offers improved overall performance through better controllability.

In this paper, we utilize finite element simulations to conduct an analysis aimed at identifying the sources of deviations. We then propose design alternatives to address the problem source while still keeping current design geometry and dimension specifications. The performance of the various design alternatives is then analyzed and compared through finite element simulations. The best-selected design is then fabricated and experimentally tested to validate the improvement. Lastly, we explore the new manipulator design's inverse kinematic model by employing an artificial neural network, which is trained and tested with experiments.

The main contributions of the paper include: a comprehensive analysis of the source of the deviations; an improved novel design of a soft robotic manipulator that minimizes deviations while still keeping the original design specifications; a new manufacturing process to fabricate a more complex design of soft robotic manipulator; and the development and testing of an artificial neural network inverse kinematic model for two DOF soft robotic manipulator.

The rest of the paper is organized as follows: Section 2 presents the problem formulation and analysis of the deviation problem. Section 3 details the new design requirements, specifications, finite element simulation comparisons, and the selection of the new design. The fabrication process of the selected design and the results of the experimental testing are presented in Section 4. Section 5 explains the development and testing of the manipulator's inverse kinematic model. Finally, Section 6 concludes the paper with remarks and outlines future works.

## 2. Problem Analysis

### 2.1. Problem formulation

The original manipulator design analyzed in this work is based on the 2 DOF manipulator described in [23], which has a tubular shape with three internal chambers spaced at  $120^\circ$  and separated by straight partition walls. It was designed to have a morphing internal structure to maximize its lateral force [12] and is equipped with two helical windings to avoid ballooning, as well as an inextensible cable sleeve at the center, to improve its lateral force. The manipulator has a total length of 76 mm, which includes a 10 mm bottom cap and a 6 mm top cap. Figure 1 shows the original design manipulator and its cross-section dimensional specifications.

The manipulator is composed of several distinct parts, namely the main body, the fiber winding, and the central rod. The main body and central rod exhibit perfect symmetry every  $120^\circ$ , while the fiber winding remains as the sole asymmetrical component at  $120^\circ$ . In the original design, the fiber winding is constructed with two helical windings wound in clockwise and counterclockwise directions, a configuration commonly employed in other works [24, 25]. While this winding shape avoids generating a twisting effect [26], it achieves symmetry only every  $180^\circ$ .

In several different works, including [14], it has been observed that during single-chamber pressurization of the original design, the manipulator tends to skew to the side, leading to a change in its plane of bending (as can be seen in Figure 2(b)). This issue occurs in each of the three chambers, but at different pressure values and in different directions. Given the asymmetrical nature of the winding used, it is highly likely that the windings contribute to the deviation in the bending plane to some extent. The effect of winding on the single-chamber pressurization bending of 2 DOF manipulators has been investigated in [23], where it was concluded that the intersection position of the two helical windings affects the stiffness of each chamber. Building upon this insight, it is hypothesized that when the intersection of the winding is not perfectly positioned above a particular chamber, the stiffness of that chamber can increase on one side, leading to the tendency of the manipulator to skew. However, this

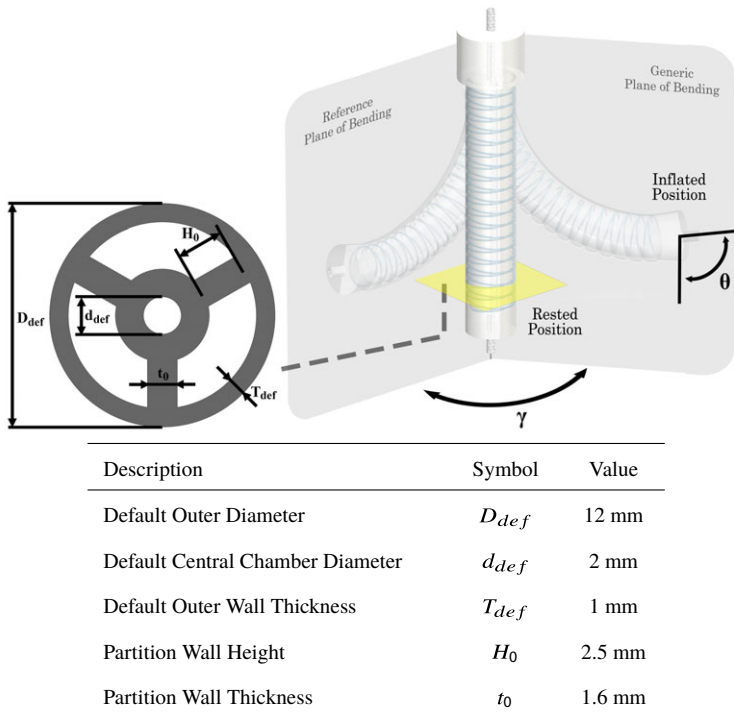


**Figure 1.** Original design manipulator and cross-section dimensional specifications.  $\gamma$  and  $\theta$  depict the bending plane orientation angle and the bending angle of the manipulator when actuated.

hypothesis fails to fully explain the observed deviation, as one of the chambers in the original design is located directly below the intersection and should not experience any asymmetrical nature of the winding.

Another hypothesized source of deviation is the buckling of the partition wall. Due to the morphing inner structure feature, during single-chamber pressurization, the partition wall located directly opposite the pressurized chamber would experience a compressive load. According to Euler’s buckling theorem, this load can cause the partition wall to buckle when it reaches a critical value. This hypothesis provides an explanation for the deviation observed in chambers with symmetrical features. It would also explain the sudden decrease in bending stiffness reported in [23] and the different values of bending plane orientation angles observed in [14] when the manipulator is continuously pressurized in clockwise and counterclockwise orders.

In the following section, we will further investigate these two hypotheses through finite element simulations to confirm the root cause of the bending plane deviation problem.

### 2.2. Finite element analysis

The finite element models were developed in Abaqus/Standard (Simulia™; Dassault Systèmes, Vélizy-Villacoublay, France), following the procedures, configurations, and material coefficients outlined in [23], which optimize convergence and computation time. It is important to note that the models were carefully meshed using a specific model partition pattern, with meticulous attention given to the mesh number and quality. The goal was to achieve a perfectly symmetrical and uniform meshing every 120° to ensure that there are no variations in stiffness caused by the mesh, which could potentially lead to a misinterpretation in the analysis.

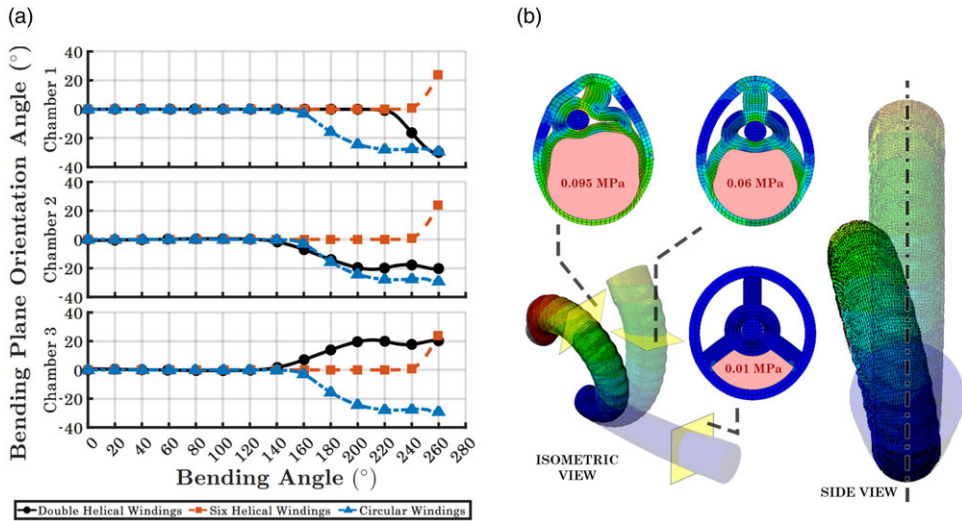


**Figure 2.** Original design simulation results. (a) Bending plane orientation angle ( $\gamma$ ) versus bending angle ( $\theta$ ) of the manipulator with different types of winding. (b) The manipulator and its cross-section during pressurization at three different pressure values given to one of the chamber (depicted with red shading).

### 2.2.1. Winding's asymmetry analysis

To investigate the winding hypothesis, we simulated the original design with its two helical windings, as well as other types of windings that have been tested in [23] to preserve the bending stiffness across different chambers. These options include a circular winding, which is completely symmetrical for every angle, and a six helical winding, a winding type with three pairs of helical windings arranged to be separated  $120^\circ$  apart, making it symmetrical for a three-chamber manipulator also spaced 120 degrees apart (see [23] for details). Each chamber was subjected to a pressure ramped up to 0.1 MPa, and the deviation was monitored through the bending plane orientation angle ( $\gamma$ ). Figure 2(a) shows the relationship between the bending plane orientation angle ( $\gamma$ ) and the bending angle ( $\theta$ ) for each chamber and different fiber winding shapes.

The simulation results indicate that the manipulator with six helical windings performed the best, deviating at higher bending angles in all chambers. In comparison, circular winding only outperformed the original double helical windings in chambers 2 and 3. These results reveal that, even with symmetrical winding shapes, the manipulator still exhibits a tendency to skew to the side. When comparing the data from symmetrical windings to the original asymmetrical winding, it becomes evident that asymmetry contributes to the deviation in the bending plane.

Firstly, looking at the chamber 2 and 3 performances, we could observe improvement from the manipulator with symmetrical windings. This could be explained by the fact that in both of these chambers, the double helical winding is asymmetric. On the other hand, at chamber 1, circular windings did not perform better than helical winding, since at this chamber, the double helical winding is symmetric, meaning the deviations here were not directly affected by the winding's symmetry.

Secondly, we observed that at chamber 2, the manipulator with double helical winding deviates to lower value, while at chamber 3 it deviated to higher value. This direction tendency happened to be the same direction of the side where the winding's asymmetry would create the least stiffness [23].

### 2.2.2. Partition Wall's buckling analysis

We investigated the hypothesis of buckling in the partition wall by simulating individual chamber pressurization of the manipulator's model with the original double-helical windings. To prevent asymmetry

in the windings from affecting the result, pressure up to 0.1 MPa was applied only to chamber 1, where the double helical winding is symmetric. We utilized the cut view feature of Abaqus/Standard during post-processing, with the follow model deformation enabled, allowing us to view the inner deformation of the manipulator during pressurization. In Figure 2(b), simulation images of the manipulator's cross-section are presented, showing the deformed state under low pressurization, medium pressurization, and high pressurization.

After closer inspection of the partition wall deformations, it is apparent that the primary cause of the observed bending plane deviation was the buckling of the partition wall. In Figure 2(a), it can be observed that the manipulator experienced a deviation in the bending plane when its bending angle reaches approximately  $220^\circ$  or around 0.09 MPa, which coincidentally corresponds to the pressure at which the compressive load applied to the partition wall opposite the pressurized chamber reached its critical point, resulting in buckling phenomena. The direction of the bending plane deviation aligns with the direction of the buckling, which, in this particular simulation, is towards the left side (as depicted in Figure 2(b)). However, it is important to note that these simulations are conducted under the assumption of perfect conditions. In real-world prototypes, we suspect that the required bending angle needs to be reached before the manipulator deviates or the direction of buckling would be significantly influenced by imperfections in the prototype or testing conditions, making it less predictable.

### 3. Design and finite element analysis

#### 3.1. Design requirements

The main cause of deviation has been identified as the buckling of the partition wall. Therefore, we propose several design alternatives aimed at preventing or reducing the impact of this phenomenon. For our new design requirements, we have retained the original major specifications, including three working chambers, a 2 mm working channel at the center, a morphing inner structure, and an outside diameter of 12 mm. These specifications allow for a simpler direct comparison between the original and the new designs. Additionally, the 12 mm outside diameter is in line with the requirements of minimally invasive medical procedures [22]. The designs should also avoid overly complicated geometry and extremely thin parts (i.e. less than 0.6 mm) to ensure the feasibility of the fabrication.

#### 3.2. Proposed designs

Before developing the new designs, we conducted further simulations on the original design's partition wall with modified dimensions, specifically with lower aspect ratios. This modification aimed to increase the wall's second moment of inertia, thus increase the critical buckling load. Through these initial simulations, we learned that while this approach increases the bending angle before deviation occurs, it also compromises the morphing feature of the original design, which allows the maximization of the chamber's cross-sectional area that leads to higher lateral force. This led us to explore other alternatives by modifying the structural shape of the partition wall.

Using structural shapes with high second moment of inertia would similarly compromise the morphing design of the manipulator. Therefore, our approach shifted to exploring shapes that allow controlled deformation of the internal chambers, allowing the chamber to expand first to maximize the total surface area before the wall receives the buckling load.

Our first option involves asymmetrical walls, which due to their asymmetry, would deform in one predefined direction, intentionally allowing bending plane deviation but in predictable direction. This sub-concept could potentially provide a simple and easy-to-manufacture solution to reduce the unpredictable impact of buckling walls. Our second option features symmetrical walls, which would be more challenging to manufacture but could completely eliminate bending plane deviation as they would symmetrically deform into a more stable shape with low aspect ratio.

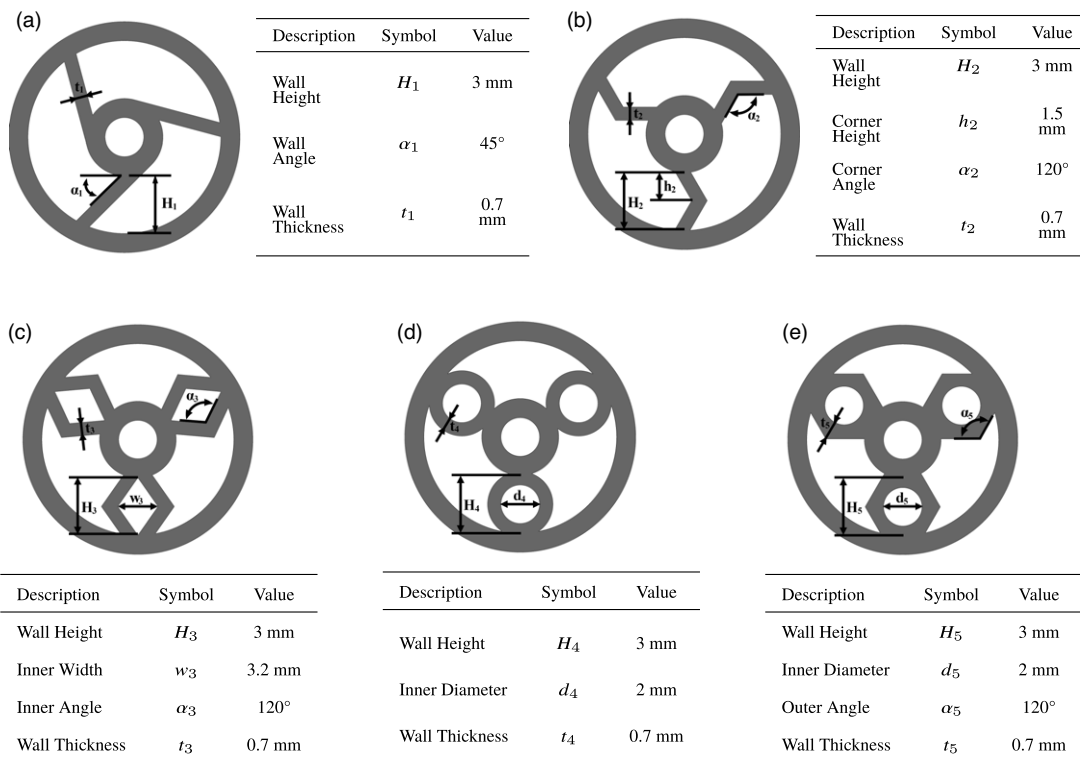


**Figure 3.** Proposed designs' cross-section geometry and dimensional specifications. (a) Proposed design 1: angled walls. (b) Proposed design 2: zig-zag walls. (c) Proposed design 3: hollow diamond walls. (d) Proposed design 4: hollow circle walls. (e) Proposed design 5: hollow hybrid walls.

In this work, we propose five alternative designs, with their geometries and dimensional specifications shown in Figure 3. The first two proposed designs use the asymmetrical deforming walls: angled walls (Figure 3(a)) and zig-zag walls (Figure 3(b)), while the remaining three designs use the symmetrical deforming walls: hollow diamond walls (Figure 3(c)), hollow circle walls (Figure 3(d)), and hollow diamond-circle hybrid walls (Figure 3(e)). All the proposed designs adhere to the design requirements mentioned in Section 3.1.

### 3.3. Finite element simulations

To evaluate the performance of the proposed designs mentioned in Section 3.2, finite-element models were again developed in Abaqus/Standard (Simulia™; Dassault Systèmes, Vélizy-Villacoublay, France), following similar configurations as the original design's model from Section 2.2. The models were simulated by pressurizing one of the chambers individually up to 0.1 MPa, and the performance was evaluated through bending plane orientation angle ( $\gamma$ ) and bending angle ( $\theta$ ). In all the new models, the original two-helical windings were still used, but only the partition wall directly opposite the chamber located exactly below the windings intersection was tested. This ensured that the winding's asymmetry would not affect the deformation of the partition wall or the expansion of the pressurized chamber to cause any buckling.

Figures 4(a) and 4(b) showcase the results of the finite element simulations for the original design and five proposed designs, including the bending plane orientation angles ( $\gamma$ ) and the bending angles ( $\theta$ ).



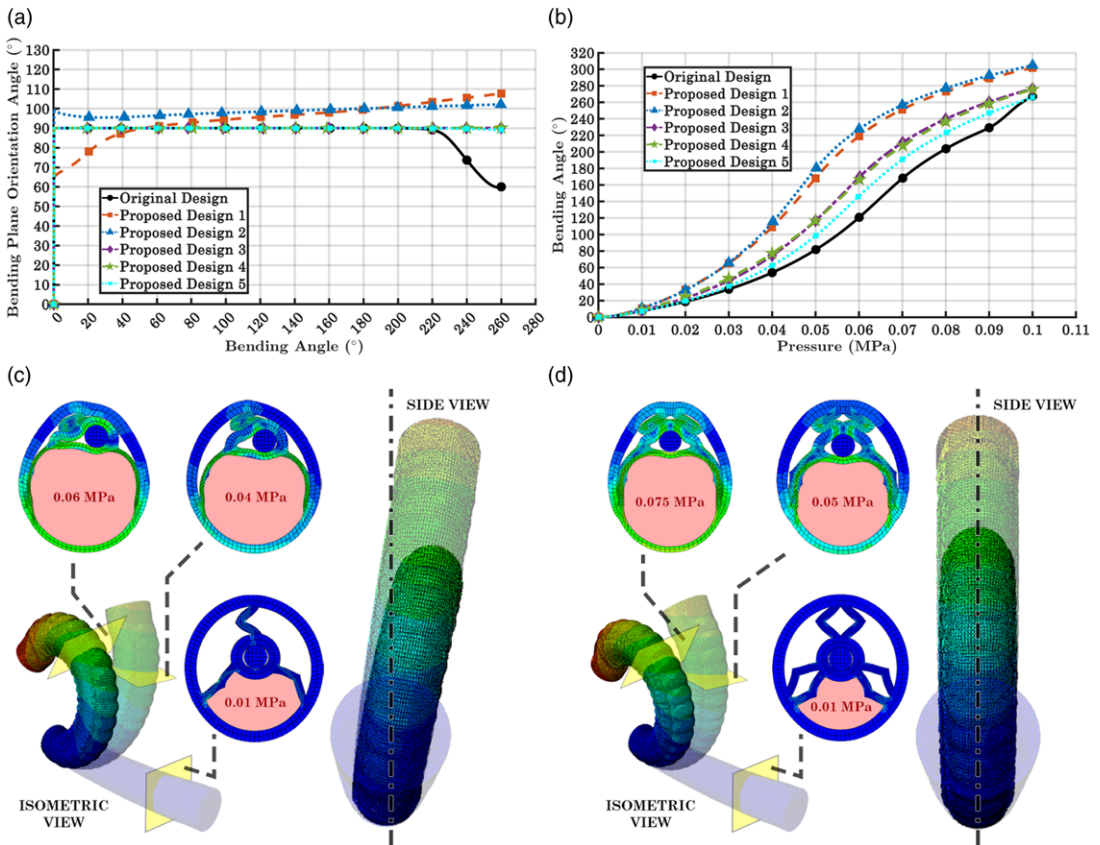


**Figure 4.** Comparison of the designs simulation results. (a) Bending plane orientation angle ( $\gamma$ ) versus bending angle ( $\theta$ ). (b) Bending angle ( $\theta$ ) versus pressure. (c) Proposed design 2 manipulator and its cross-section during pressurization. Side view of the manipulator reveals deviating but a constant bending throughout pressurization. (d) Proposed design 3 manipulator and its cross-section during pressurization.

Analyzing the cross sectional deformations of asymmetrical wall design (zig-zag wall) in Figure 4(c) shows that the wall deformed early as expected, and in one definitive direction. Furthermore, no sudden jump in bending plane orientation angle was observed, as seen in the original design (Figure 2(b)), where the manipulator would start bending in straight but suddenly deviate to the side. This proves that asymmetrical deformable walls reduce the unpredictability of the original design. Additionally, the deforming feature of the partition wall provides less resistance to the manipulator’s chamber expansion and bending, improving the manipulator’s bending angle stiffness. However, even though the bending angle orientation angle is predictable in direction, it is unstable as it continues to deviate long after the wall has fully collapsed.

For symmetrical deformable wall designs (diamond, circle, and diamond-circle hybrid wall), analyzing cross-sectional deformation and the bending angle orientation angles ( $\gamma$ ) shows that these walls collapse symmetrically, eliminating any bending plane deviation and proves to be stable up to 0.1 MPa. As the walls morph into stable shapes (Figure 4(d)), they effectively withstand the compressive load and allow for the symmetrical expansion of the pressurized chamber. Similarly, although not as much as the previous sub-concept, the symmetrical walls also provide less resistance for the chambers to expand and the manipulator to bend compared to the original design.

### 3.4. Design selection

In order to select the best design for experimental testing, we conducted a thorough evaluation of several key parameters based on the bending plane orientation angle, bending angle, and the manufacturing process. We used a relative comparison method with a quantitative approach to assist in the design selection process.

With this method, weights were initially assigned to each of the key performance parameters, with higher values indicating greater importance. We then evaluated each of the proposed designs across all relevant parameters, assigning scores from 0 to 1 on the corresponding scale ( $N_i$ ), and calculated the weighted score or rating ( $R_i$ ) by multiplying these scores with the predetermined weights ( $R_i = N_i \times \text{weight}$ ). The overall score for each proposed design was then obtained by adding these final ratings.

Taking into account the main aim of this study, we set the parameter with highest priority as the  $\gamma$  slope and  $\gamma$  slope consistency. Bending stiffness was prioritized next, being a common parameter for evaluating the performance of a manipulator. Fabrication complexity and mold complexity were equally prioritized next, as both have a direct impact on the prototype quality and, hence, the final experimental performance.

To determine the corresponding scales quantitatively, we used equations (1), (2), (3), (4), and (5), which were based on the relative differences of the proposed design compared to the original design. The gamma slope and slope consistency corresponding scale ( $N_{(j,1)}$  and  $N_{(j,2)}$ ) were calculated based on the simulated bending plane orientation angle gradient, while bending stiffness ( $N_{(j,3)}$ ) was based on ( $\theta$ ) versus pressure curve, ranging from 0 to 260°. Similarly, both fabrication ( $N_{(j,4)}$ ) and molds complexity ( $N_{(j,5)}$ ) were determined by penalizing the score for every additional step or additional custom mold parts required.

$$N_{(j,1)} = 0.5 - \frac{1}{2} \frac{\frac{1}{n} \sum_{i=1}^n \nabla \gamma_j - \frac{1}{n} \sum_{i=1}^n \nabla \gamma_0}{\frac{1}{n} \sum_{i=1}^n \nabla \gamma_0} \tag{1}$$

$$N_{(j,2)} = 0.5 - \frac{1}{2} \frac{\frac{1}{n} \sum_{i=1}^n \Delta(\nabla \gamma_j) - \frac{1}{n} \sum_{i=1}^n \Delta(\nabla \gamma_0)}{\frac{1}{n} \sum_{i=1}^n \Delta(\nabla \gamma_0)} \tag{2}$$

$$N_{(j,3)} = 0.5 + \frac{1}{2n} \sum_{i=1}^n \frac{\theta_{j,i} - \theta_{0,i}}{\theta_{0,i}} \tag{3}$$

$$N_{(j,4)} = 1 - \frac{n_{(j,s)} - n_{(0,s)}}{n_{(0,s)}} \tag{4}$$

$$N_{(j,5)} = 1 - \frac{n_{(j,p)} - n_{(0,p)}}{n_{(0,p)}} \tag{5}$$

where  $\nabla \gamma_j$  and  $\nabla \gamma_0$  are the slope of the bending plane orientation angles of the proposed design  $j$  and the original design, respectively.  $\theta_j$  and  $\theta_0$  are the bending angles of the proposed design  $j$  and the original design, respectively.  $n_{(j,s)}$  and  $n_{(j,p)}$  are the number of steps and the number of custom parts required to manufacture the proposed design  $j$ , respectively.  $n_{(0,s)}$  represents the original design’s number of manufacturing steps, which in this work is set to four: initial molding, fiber winding, outer layer molding, and final sealing.  $n_{(0,p)}$  is the number of parts in the original design molds, which include eight parts: a one-part inner mold, a two-part initial outer mold, a two-part final outer mold, and a three-part final sealing mold.

Table I outlines our relative comparison analysis of the proposed designs. Based on this analysis, proposed design 3 and 4 have the highest calculated rating value of 0.81. In this study, we selected proposed design 3 for fabrication and experiment testing, since its cross-sectional geometry involves fewer tight angles compared to the proposed design 4, offering easier fabrication. Furthermore, the diamond shape



*Table I. Relative comparison table*

Parameters	Weight	Proposed design 1		Proposed design 2		Proposed design 3		Proposed design 4		Proposed design 5	
		$N_{(j,1)}$	$R_{(j,1)}$	$N_{(j,2)}$	$R_{(j,2)}$	$N_{(j,3)}$	$R_{(j,3)}$	$N_{(j,4)}$	$R_{(j,4)}$	$N_{(j,5)}$	$R_{(j,5)}$
Gamma Slope	0.30	0.34	0.10	0.77	0.23	1.00	0.30	1.00	0.30	0.99	0.30
Gamma Slope	0.30	0.75	0.23	0.94	0.28	1.00	0.30	1.00	0.30	0.99	0.30
Consistency											
Bending Stiffness	0.20	0.76	0.15	0.76	0.15	0.59	0.12	0.57	0.11	0.48	0.10
Fabrication	0.10	1.00	0.10	0.75	0.08	0.50	0.05	0.50	0.05	0.50	0.05
Complexity											
Molds Complexity	0.10	1.00	0.10	0.63	0.06	0.38	0.04	0.50	0.05	0.50	0.05
Total Rating			0.68		0.78		0.81		0.81		0.80

(proposed design 3) was also expected to provide greater stability when deforming due to its geometry, which should help improve the prototype’s performance, compensating for any imperfections in the prototype.

#### 4. Experimental validation

##### 4.1. Manufacturing process

The original design prototypes were fabricated using the process and mold sets described in [23]. The resulting prototype possesses the specifications, material, and winding shape of the simulations.

On the other hand, the new design prototype was manufactured using a more complex process and special mold sets, as its design presented a set of new challenges. The main challenge arose from its intricate and relatively small geometry, which necessitated molds consisting of multiple parts that were difficult to manufacture. This complex geometry also posed a de-molding issue, as the inner mold required had a larger surface area, resulting in increased friction. Another challenge stemmed from the hollow parts of the design, which required exhaust holes to prevent the trapping of air when the partition wall collapsed, further complicating the process. Bearing all of these factors in mind, a three-part mold and another two-part mold (shown in Figure 5(b)) were used. This three-part mold was used to fabricate the main body, complete with its fiber winding, bottom cap, and exhaust holes for the partition wall at the bottom, while the additional two-part mold was used to add the final top sealing cap on the main body and was manufactured with the 3D printer.

For the three-part mold, the first main part was the smaller outer mold consisting of two constituent parts, featuring grooves in its inner surface to create a path for an exact double-helical winding and manufactured using a conventional 3D printer (Objet500, Stratasys, Ltd., Israel). The second main part was the larger outer mold, which was also manufactured using a conventional 3D printer, but contrary to its smaller counterpart, it didn’t feature any grooves and had a slightly larger inner diameter. The third main part is the inner mold, comprising a bottom mold that holds a 2 mm high-speed steel rod, three pieces of chamber shafts, and three pieces of partition wall shafts. All of the inner mold parts were manufactured using a wire EDM cutting process, allowing the fabrication of precise and low-tolerance parts.

Figure 5(a) illustrates the overall manufacturing process for the new design. The first step involved assembling the inner mold with all its constituent parts, which was then placed inside the smaller outer mold. Following a similar process to the original design, the silicone-rubber material Dragon Skin™ 10 Medium (Smooth-On, Inc., Pennsylvania, USA) was injected into the smaller outer mold, resulting in the production of the bottom cap and main body of the manipulator (as can be seen in Figure 5(a)-1).

Next, the fiber thread was manually wound around the main body, following the guide path to create perfect double-helical windings (as shown in Figure 5(a)-2). Once completed, the specimen was placed

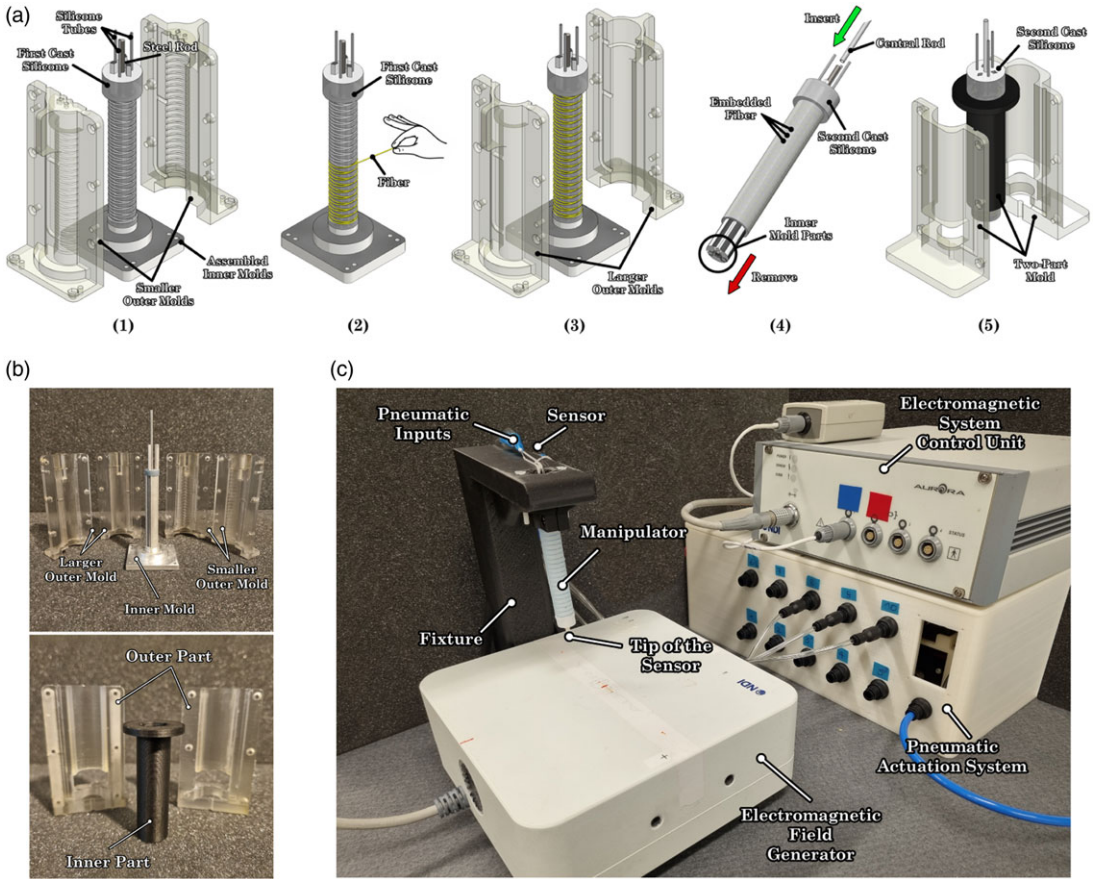


**Figure 5.** (a) Manufacturing process of the proposed design. (b) The three-part and two part mold of the proposed design. (c) Experimental setup.

inside the larger outer mold and re-injected with silicone-rubber material to secure the windings in place (shown in Figure 5(a)-3). Due to the presence of chamber shafts in the inner mold, the resulting cast already featured three exhaust holes located at the bottom cap.

Finally, the inner mold with all its constituent parts was removed, an inextensible central rod was inserted, and the two-part mold was used to seal the top of the prototype (as can be seen in Figure 5(a)-4 and 5(a)-5). This final sealing process required meticulous attention to ensure that all of the seven chambers were separated.

#### 4.2. Experimental setup

The experiments were conducted by clamping the bottom cap of the prototypes upside down on a fixture (as can be seen in Figure 5(c)). The rest of the setup followed a similar configuration described in [27], where an aurora electromagnetic 5 DoF sensor was fixed at the tip of the manipulator, and its position and rotation were measured using an electromagnetic tracking system (Aurora, NDI, Canada, 0.70 RMS).

Prior to the experiment, a calibration process was performed by actuating Chamber 1 at 0.05 MPa. A custom script was used to record the sensor's rotation matrix before ( $\mathbf{R}_{\text{ref},1}$ ) and after actuation ( $\mathbf{R}_{\text{ref},2}$ ). The bending plane identified during the calibration was later used as the reference plane for measuring  $\gamma$ .

In this work, we performed two types of pressurization for each prototype. These included individual chamber pressurization up to 0.1 MPa in each of the three chambers and two chambers vectorization. The vectorization process included pressurizing different combinations of chambers, each with various pressure ratios. After each step, both chambers were depressurized. A pneumatic actuation system, comprising proportional pressure regulators (Tecno Basic, Hoerbiger, Germany), as mentioned in [27], was utilized to pressurize the prototypes as needed.

For each data point, a new rotation matrix was obtained 3 s after the pressurization, ensuring quasi-static condition. Performance was evaluated by calculating the bending angle ( $\theta$ ) and the bending plane orientation angle ( $\gamma$ ), using equation 6 and 7, respectively.

$$\theta = 2 \cos^{-1} (q_{\text{ref},1} \cdot q_m) \tag{6}$$

$$\gamma = \cos^{-1} \left( \frac{\hat{n}_m \cdot \hat{n}_{\text{ref}}}{\|\hat{n}_m\| \cdot \|\hat{n}_{\text{ref}}\|} \right) \tag{7}$$

where  $q_{\text{ref},1}$  and  $q_m$  are the quaternions corresponding to  $\mathbf{R}_{\text{ref},1}$  and  $\mathbf{R}_m$ , respectively. Instead  $\hat{n}_{\text{ref}}$  and  $\hat{n}_m$  are the normal vector of the reference bending plane and measurement bending plane, respectively.

### 4.3. Results comparison and discussion

Figure 6(a) illustrate the performance of both prototypes during individual chamber pressurization in each of the three chambers. Figure 6(b) compares the relations between the bending plane orientation angle and bending angle of the original and new design prototypes.

Upon comparing the original and the new design, improvements in the bending plane angle orientation angle ( $\gamma$ ) were observed. The angles of chamber 1 and chamber 3 in the new design prototype were noticeably more stable, reaching a higher bending angle ( $\theta$ ) before  $\gamma$  deviated. However, the pressurization of chamber 2 resulted in little to no improvement in terms of deviation and only reached around 110° in  $\gamma$ , slightly lower than expected. Additionally, at the maximum of the pressure range, the new design prototype still exhibited a slight deviation, although it only occurred at pressures exceeding 0.075 MPa, where the bending angle had almost reached 180°. It is believed that this reduced improvement compared to the simulations could be attributed to the larger manufacturing errors of the new design compared to the initial prototype, since it involved additional steps and mold components.

Furthermore, when comparing the bending angle stiffness ( $\theta$ ) of both prototypes, it is evident that the new design possesses a more optimal stiffness. In all three chambers, the new design prototype managed to reach higher bending angles at lower pressure, while being surpassed by the original design at higher pressure. We believe the improvement in the experiment is less significant due to the thicker outer walls of the new design prototype as a result of imperfect molds, and the overtake was the result of the gradual decrease in stiffness that occurred in the original design due to buckling.

In conclusion, looking at the individual chamber pressurization performance, although the improvement of the new design may not be as significant as observed in simulations, it still demonstrates sufficient improvement for most practical applications.

The prototypes' vectorization for a full 360° rotation of bending planer orientation angle is depicted in Figure 6(c). It was obtained by pressurizing specific combinations of chambers at specific ratio. Comparing them with the theoretical optimal  $\gamma$  based on the vectorization models described in [27], result an MAE of  $8.20 \pm 5.16$  for the original design, and  $8.83 \pm 6.36$  for the proposed design prototype.

Looking at the overall vectorization error of both prototypes, it can be observed that the bending plane orientation angle of the new design is comparable to that of the original design. The new design has slightly higher deviations relative to the theoretical  $\gamma$  values. This could be attributed to the higher error at ratios where one of the chambers has a significantly lower pressure compared to the other chamber. The main reason for this is likely related to the stabilizing effect of the diamond shape partition when collapsing, which helps prevent deviation during individual chamber pressurization but unintentionally pulls the bending plane towards one of the chamber's bending planes during vectorization. Although

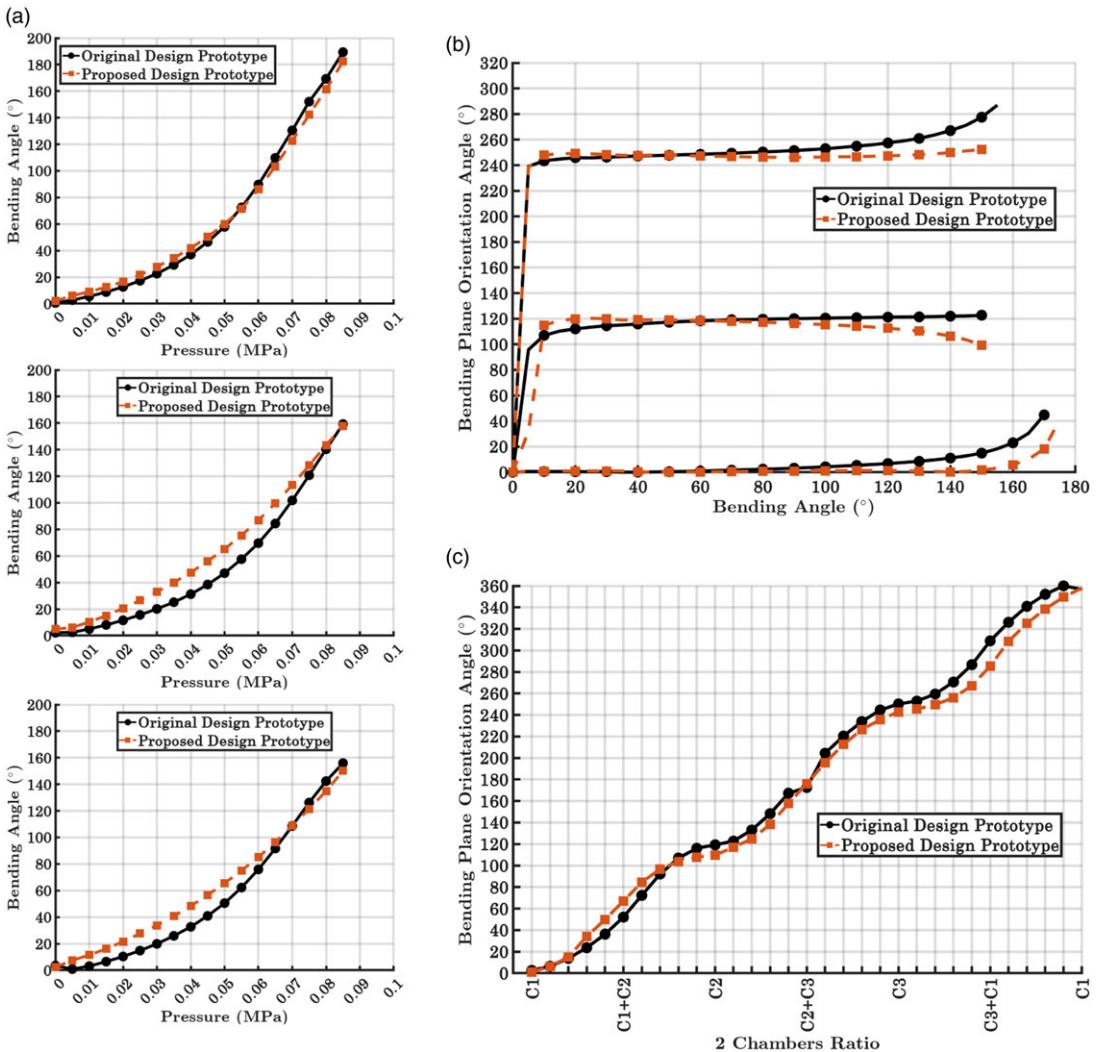


**Figure 6.** Experimental results comparison of original and proposed design. (a)  $\theta$  versus pressure for chamber 1 (top), chamber 2 (middle), and chamber 3 (bottom) (b)  $\gamma$  versus  $\theta$  for each chamber pressurization. (c) vectorization performance -  $\gamma$  versus order of pressurized chamber.

this characteristic may not be desirable, the effect is predictable and repeatable, and therefore it can be mitigated by implementing a non-linear ratio-to- $\gamma$  control policy.

Overall, despite the new design requiring a more complex manufacturing process and exhibiting higher non-linearity during vectorization, it also demonstrates superior performance in terms of deviation resistance and bending stiffness.

### 5. Inverse Kinematics

The experiment outlined in Section 4 made it apparent that the new design requires a more complex inverse kinematic model for specific movements, such as vectorization. Additionally, due to the collapsible partition wall, the new design would have higher inner structure deformation, thereby increasing its non-linearity and complexity. With these reasons in mind, we employ an artificial neural network, which

has been proven to perform well both in the design and control of soft devices [28, 29], to obtain the inverse kinematics model for the new manipulator design. This approach has the potential to effectively capture the nonlinear characteristics of soft manipulators, especially in an open-loop scenario, without relying on complex analytical models or on restrictive assumptions. We then utilize this model to demonstrate improved intermittent vectorization in the prototype of the new design.

### 5.1. Artificial neural network model

In this work, we aim to build an artificial neural network to solve the inverse kinematic problem of the manipulator, relating its angles with the respective combinations of pressure inputs in quasi-static conditions. Considering the relative simplicity of the problem, we designed a simple deep neural network architecture with three hidden layers, two inputs for the target bending angle ( $\theta$ ) and target bending plane orientation angle ( $\gamma$ ), and three outputs for the predicted pressure in each of the chambers ( $P_1, P_2, P_3$ ). Through k-fold validations, we empirically set the number of neurons for each of the hidden layers to be 16, 8, and 4, with the *tanh* activation function used in each of the layers.

Each data point for the training data sets was obtained by randomly applying pressure combinations in the manipulator's chambers, respecting the following conditions: pressure input values were in the range of 0.01 to 0.08 MPa; at least one of the chambers in each segment remained unactuated; the pressurization sequence was given in an intermittent fashion, where the manipulator was returned to the unactuated state before the next values were applied; data points were recorded after a 3-second delay to ensure a steady-state condition. In total, 600 data pairs containing the given pressure combinations and the manipulator's angles were recorded.

### 5.2. ANN model training and testing

To generalize the performance of the trained model, k-fold validation with ( $k = 12$ ) was utilized. In this method, the training data set was split into 12 batches, each containing 50 different data pairs. Model training was repeated 12 times, with each iteration using eleven batches for training, and one remaining batch was used for validation. Each batch would serve as the validation set exactly once. The objective of the training was to optimize the network's weights and biases using the adaptive moment estimation algorithm, minimizing the mean square error between the network's predictions and the actual target data. The performance metrics from all repetition were averaged to obtain the generalized performance of the trained model. Through this process, we obtained the model validation performance with an  $R^2$  score of  $0.98 \pm 0.01$  and a mean absolute error (MAE) of  $0.03 \pm 0.01$ .

Experimental validation was performed using the model with the closest MAE value with the average performance. Testing was conducted to predict pressure input values of 100 random combinations of  $\theta$  and  $\gamma$ , with a range of  $10^\circ$  to  $120^\circ$  for the  $\theta$ . Figure 7(a) and Figure 7(c) display the final models' actual versus target  $\gamma$  and  $\theta$ , respectively.

In the experimental validation, the model managed to achieve  $R^2$  score of 0.998 and MAE of  $4.16 \pm 2.24$  for  $\gamma$  prediction, and  $R^2$  score of 0.95 and MAE of  $3.93 \pm 3.19$  for  $\theta$  prediction. The ANN model was capable of predicting the necessary combination of pressure for two chambers to achieve specific target  $\theta$  and target  $\gamma$  values with relatively low MAE errors. Significant improvements, up to 5 degrees, could be observed in the MAE error of  $\gamma$  when we compare it to the vectorization performance of the new prototype without the ANN model (shown in Section 4.3).

To gain a better understanding of the model's performance, we also investigated the combinations of  $\theta$  and  $\gamma$  where the model faced the most difficulties in making accurate predictions. Figure 7(b) and Figure 7(d) display an error heat map of target  $\theta$  and  $\gamma$  combinations that resulted in higher errors of actual  $\gamma$  and  $\theta$ .

Analyzing the heat maps, we observed that higher  $\theta$  errors mostly occur around high  $\theta$  targets. This is most likely caused by the increased non-linearity of the manipulator at high bending angle, making it less predictable. On the other hand, high  $\gamma$  errors mostly occur at low  $\theta$  targets. This was most likely



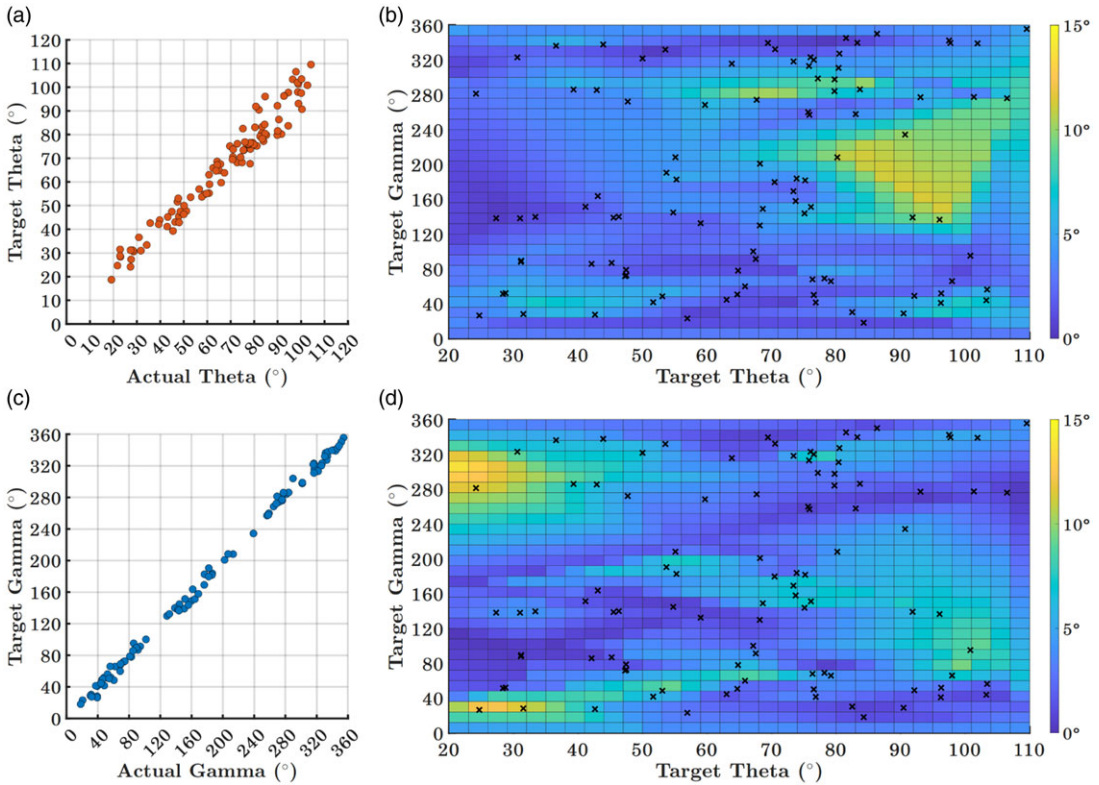


**Figure 7.** Neural network experimental validation results. (a) Target versus actual measured  $\theta$ . (b) Target versus actual measured  $\gamma$ . (c) Error heat map of  $\theta$ . (d) Error heat map of  $\gamma$ . Error grids were generated through linear interpolation using the recorded data points (depicted as cross markers).

caused by the limitations in the experimental setup, which faced difficulties in accurately measuring  $\gamma$  when the bending angle is too low.

Nevertheless, we find that the inverse kinematics model based on ANN shows promise and demonstrates the potential of the new design. However, it also comes with some challenges that may require further improvement in future works. One of the challenges is the high number of training data points required for the model, which could potentially reduce the prototype's life expectancy.

## 6. Conclusions

This paper presents a comprehensive analysis and design optimization process for a 2 DOF tubular soft manipulator design using finite element simulations. We identified the sources of the design's bending plane deviation in our previous work as the buckling phenomena of the partition wall and proposed design alternatives to address the problem while maintaining the current geometry and dimension specifications. The alternatives were tested and compared through simulations, and the best-selected design, with a diamond-shaped partition wall was chosen. Subsequently, both the original and selected design prototypes were manufactured, thoroughly tested, and compared through experiments.

During individual chamber pressurization testing, two out of three chambers in the selected design exhibited improvements in bending angle values before deviating. All of the chambers also showed improved bending stiffness compared to the original design, although they were occasionally surpassed by the original design at higher pressures due to a decrease in stiffness caused by the buckling of the partition wall. Reduced improvements were observed compared to the simulation, most likely due to



the lower quality of the new design prototype compared to the original, which was the result of a more complex manufacturing process. In future work, improving the manufacturing process to require fewer steps or molds might enhance the prototype tolerances and overall performance. Alternative materials could also be explored to enable the use of additive manufacturing processes.

In the vectorization experiments, the new design showed slightly higher deviation in bending plane orientation compared to the theoretical value. This effect was attributed to the stabilizing influence of the diamond-shaped partition during collapsing, unintentionally affecting the bending plane orientation. Nonetheless, the non-linear bending plane orientation is repeatable and predictable, and can thus be compensated for with an appropriate control policy. Consequently, we developed and implemented an artificial neural network-based inverse kinematics model which proved capable of predicting the necessary pressure combinations for target  $\theta$  and  $\gamma$  values yielding relatively low RMS errors. However, optimizing the model's high demand for training data points may be necessary to improve its efficiency and extend the prototype's life expectancy. Being trained on a specific prototype might also reduce the generalizability of the model, restricting its application. To this end, in the future, we are planning to explore the possibility of reusing a trained model by employing transfer learning strategies.

In summary, the new manipulator design showcased significant improvements in deviation resistance, bending stiffness, and consistent  $\gamma$  values during vectorization. Despite encountering some challenges, the results indicate the promising potential of this design for practical applications. In future work, we plan to further improve manufacturing to achieve higher consistency in wall thickness, both in the outer wall and partition walls. We also plan to fabricate a soft robotic manipulator made of 2 segments with the new design proposed in this work and to develop direct and inverse kinematics as well as control using extensions of the machine learning work presented in this work.

**Author contributions.** Conceptualization: AGC, VV; Methodology: VF, VV, AGC; Formal analysis and investigation: VF, VV, AGC; Writing - original draft preparation: VF; Writing - review and editing: VF, VV, AGC, EF, FRYB; Funding acquisition: VV, I; Resources: FRYB, I, AIM; Supervision: AGC, VV, I, EF, FRYB, AIM. All authors commented on previous versions of the manuscript. All authors read and approved the final manuscript.

**Financial support.** This work was supported by Riset ITB 2023 Program administered by Institut Teknologi Bandung and by a Newton Fund Institutional Links grant, ID 623531377, under the Newton Fund Indonesia partnership funded by the UK Department for Business, Energy and Industrial Strategy

**Competing interests.** The authors declare no conflicts of interest exist.

**Ethical statement.** Not applicable.

## References

- [1] S. Neppalli, B. Jones, W. McMahan, V. Chitrakaran, I. Walker, M. Pritts, M. Csencsits, C. Rahn and M. O. Arm Grissom, "A soft robotic manipulator," *IEEE/RSJ International Conference On Intelligent Robots And Systems*, San Diego, USA (2007).
- [2] T. Wen, J. Hu, J. Zhang, X. Li, S. Kang and N. D. Zhang, "Performance analysis, and experiments of a soft robot for rescue," *J. Mech. Robot.* **16**(7), 071011 (2024).
- [3] X. Zhang, T. Pan, H. Heung, P. Chiu and Z. Li. "A Biomimetic Soft Robot for Inspecting Pipeline with Significant Diameter Variation," **In: IEEE/RSJ International Conference On Intelligent Robots And Systems (IROS)**, Madrid, Spain (2018).
- [4] Z. Liu, Y. Wang, J. Wang, Y. Fei and Q. Du, "An obstacle-avoiding and stiffness-tunable modular bionic soft robot," *Robotica* **40**(8), 2651–2665 (2022).
- [5] N. Zhu, H. Zang, B. Liao, H. Qi, Z. Yang, M. Chen, X. Lang and Y. Wang, "A quadruped soft robot for climbing parallel rods," *Robotica* **39**(4), 686–698 (2020). doi: [10.1017/s0263574720000661](https://doi.org/10.1017/s0263574720000661).
- [6] Y. Li, Y. Wang, S. Yuan and Y. Fei, "Design, modeling, and control of a novel soft-rigid knee joint robot for assisting motion," *Robotica* **42**(3), 1–16 (2024).
- [7] M. Cianchetti, T. Ranzani, G. Gerboni, I. Falco, C. Laschi and A. Menciassi, "STIFF-FLOP surgical manipulator: Mechanical design and experimental characterization of the single module," **In: IEEE/RSJ International Conference On Intelligent Robots And Systems**, Tokyo, Japan (2013).

- [8] J. F. Ahmed, E. Franco, F. Y. B. Rodriguez, A. Darzi and Patel N., "A review of bioinspired locomotion in lower GI endoscopy," *Robotica* 1–11 (2024). doi: [10.1017/s0263574724000055](https://doi.org/10.1017/s0263574724000055).
- [9] G. Chen, M. Pham, T. Maalej, H. Fourati, R. Moreau and S. Sesmat, *A Biomimetic Steering Robot for Minimally Invasive Surgery Application* (In-Tech, Ernest Hall, 2009).
- [10] K. Suzumori, S. Iikura and H. Tanaka, "Development of flexible microactuator and its applications to robotic mechanisms," **In: Proceedings IEEE International Conference On Robotics And Automation**, Sacramento, CA, USA (1991).
- [11] S. Treratanakulchai, E. Franco, A. Garriga-Casanovas, H. Minghao, P. Kassanos and F. Baena, "Development of a 6 DOF Soft Robotic Manipulator with Integrated Sensing Skin," **In: IEEE/RSJ International Conference On Intelligent Robots And Systems (IROS)**, Kyoto, Japan (2022).
- [12] A. Garriga-Casanovas, I. Collison and F. Baena, "Toward a common framework for the design of soft robotic manipulators with fluidic actuation," *Soft Robot.* **5**(5), 622–649 (2018).
- [13] Garriga-Casanovas, A., Treratanakulchai, S., Franco, E., Zari, E., Ferrandy, V., Viridyawan, V. & Baena, F., "Optimised Design and Performance Comparison of Soft Robotic Manipulators," **In: 7th International Conference On Mechanical Engineering And Robotics Research (ICMERR)**, Krakow, Poland (2022).
- [14] V. Viridyawan, T. Ayatullah, A. Sugiharto, E. Franco, A. Garriga-Casanovas, A. Mahyuddin, F. Baena and Indrawanto, "Design and Manufacturing of an Affordable Soft-Robotic Manipulator for Minimally Invasive Diagnosis," **In: 7th International Conference On Robotics And Automation Engineering (ICRAE)**, Singapore (2022).
- [15] E. Franco, A. Casanovas, F. Baena and A. Astolfi, "Model based adaptive control for a soft robotic manipulator," **In: IEEE 58th Conference On Decision And Control (CDC)**, Nice, France (2019) pp. 1019–1024.
- [16] E. Franco, A. Casanovas and A. Donaire, "Energy shaping control with integral action for soft continuum manipulators," *Mech. Mach. Theory* **158**, 104250 (2021).
- [17] E. Franco, A. Garriga-Casanovas, J. Tang, F. Baena and A. Astolfi, "Adaptive energy shaping control of a class of nonlinear soft continuum manipulators," *IEEE/ASME Trans. Mechatron.* **27**(1), 280–291 (2022).
- [18] E. Franco, T. Ayatullah, A. Sugiharto, A. Garriga-Casanovas and V. Viridyawan, "Nonlinear energy-based control of soft continuum pneumatic manipulators," *Nonlinear Dynam.* **106**(1), 229–253 (2021).
- [19] E. Franco, A. Casanovas, J. Tang, F. Baena and A. Astolfi, "Position regulation in cartesian space of a class of inextensible soft continuum manipulators with pneumatic actuation," *Mechatronics* **76**, 102573 (2021).
- [20] T. Thuruthel, E. Falotico, F. Renda and C. Laschi, "Model-based reinforcement learning for closed-loop dynamic control of soft robotic manipulators," *IEEE Trans. Robot.* **35**(1), 124–134 (2018).
- [21] T. George Thuruthel, Y. Ansari, E. Falotico and C. Laschi, "Control strategies for soft robotic manipulators: A survey," *Soft Robot.* **5**(2), 149–163 (2018).
- [22] M. Runciman, A. Darzi and G. Mylonas, "Soft robotics in minimally invasive surgery," *Soft Robot.* **6**(4), 423–443 (2019).
- [23] V. Ferrandy, F. Indrawanto, F. Sugiharto, A. Franco, E. Garriga-Casanovas, A. Mahyuddin, A. Baena, F. Mahradi, S and V. Viridyawan, "Modeling of a two-degree-of-freedom fiber-reinforced soft pneumatic actuator," *Robotica* **41**(12), 1–19 (2023).
- [24] B. Zhang, Y. Fan, P. Yang, T. Cao and H. Liao, "Worm-like soft robot for complicated tubular environments," *Soft Robot.* **6**(3), 399–413 (2019).
- [25] G. Decroly, B. Mertens, P. Lambert and A. Delchambre, "Design, characterization and optimization of a soft fluidic actuator for minimally invasive surgery," *Inter. J. Comp. Assis. Radio. Surg.* **15**(2), 333–340 (2020).
- [26] K. Suzumori, "Elastic materials producing compliant robots," *Robot. Auton. Sys.* **18**(1-2), 135–140 (1996).
- [27] E. Franco and A. Garriga-Casanovas, "Energy-shaping control of soft continuum manipulators with in-plane disturbances," *Inter. J. Robot. Res.* **40**(1), 236–255 (2021).
- [28] A. Forte, P. Hanakata, L. Jin, E. Zari, A. Zareei, M. Fernandes, L. Sumner, J. Alvarez and K. Bertoldi, "Inverse design of inflatable soft membranes through machine learning," *Adv. Funct. Mater.* **32**(16), 2111610 (2022).
- [29] D. Kim, S. Kim, T. Kim, B. Kang, M. Lee, W. Park, S. Ku, D. Kim, J. Kwon, H. Lee, J. Bae, Y. Park, K. Cho and S. Jo, "Review of machine learning methods in soft robotics," *PLOS One* **16**(2), e0246102 (2021).